Macromolecules

pubs.acs.org/Macromolecules Article

Triblock Terpolymer Thin Film Nanocomposites Enabling Two-Color Optical Super-Resolution Microscopy

Wennie Yun Lee,[†] Dana V. Chapman,[†] Fei Yu,[†] William R. T. Tait, R. Paxton Thedford, Guillaume Freychet, Mikhail Zhernenkov, Lara A. Estroff, and Ulrich B. Wiesner*

Cite This: *Macromolecules* 2022, 55, 9452–9464 Read Online

ACCESS | Metrics & More | Article Recommendations | Supporting Information

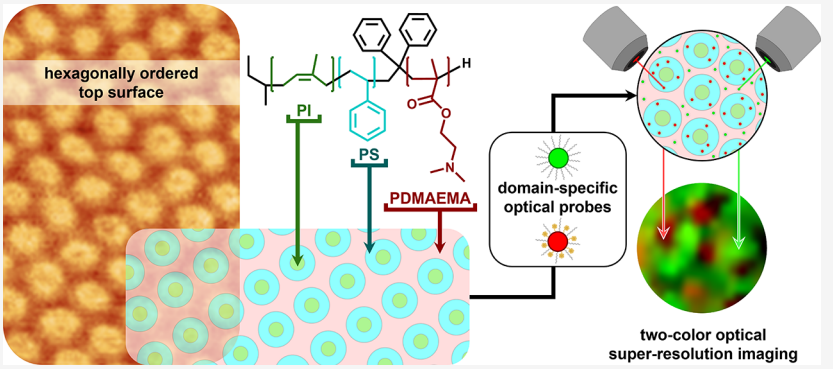

ABSTRACT: Self-assembled block copolymer (BCP) thin films and their nanocomposites provide nanostructures useful in myriad applications. While conventional characterization techniques provide an understanding of film surface and internal structures, optical super-resolution microscopy (OSRM) has recently emerged as an alternative way to characterize nanoscopic polymer morphology. This work describes self-assembled poly(isoprene)-*block*-poly(styrene)-*block*-poly(*N*,*N*-dimethylaminoethyl methacrylate) (PI-*b*-PS-*b*-PDMAEMA or ISA) triblock terpolymer thin films with all three blocks exposed at the top surface. Structural characterization of neat films with standard techniques, including grazing-incidence small-angle X-ray scattering (GISAXS), atomic force microscopy (AFM), and electron microscopy (EM), reveals a co-continuous network in the substructure of the films and hexagonally ordered top surface structures. Nanocomposite thin films incorporating two chemically and optically orthogonal core−shell optical nanoparticle probes by simple physical mixing and evaporation-induced self-assembly (EISA) retain this morphology while enabling two-color OSRM imaging of different BCP nanodomains. This approach suggests that fine-tuned organic ligand shells enable labeling of different blocks based on shell polarity, demonstrating a straightforward pathway to multicolor OSRM characterization of chemically distinct nanodomains.

INTRODUCTION

Block copolymers (BCPs) comprise a class of macromolecules composed of two or more chemically distinct polymer chains—each serving as a block—that are covalently bonded to one another. Due to enthalpy-driven microphase segregation and configurational-entropy-driven coiled block conformations, BCPs typically self-assemble on the scale of tens of nanometers to form various mesostructures at thermodynamic equilibrium.[1−3] In the bulk, relative chemical (in)-compatibility between blocks, volume fractions, total molar mass, and conformational asymmetry each play a significant role in determining BCP morphology.[4,5] Moving from bulk BCP self-assembly to thin films, the final structure is further substantially influenced by asymmetric boundary conditions——namely, the surface energy with air and the interfacial energy with the substrate.[6] Film thickness, substrate selection, film casting methods, and solvent choice also heavily influence the phase separation, morphology, and mesostructural orientation of self-assembled structures.[7,8] As a result, the development of reliable protocols for preparing and characterizing morphologically consistent films is essential to applications of BCP thin films, *e.g.*, nanopatterning or the investigation of confined reactions.[4,9]

To form well-defined morphologies, such as lamellae, gyroids, cylinders, spheres, and even more complicated structures from triblock terpolymers,[1,10−15] solvent vapor annealing (SVA) is often applied to mobilize polymer chains

Received: May 16, 2022
Revised: September 20, 2022
Published: October 17, 2022

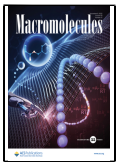

https://doi.org/10.1021/acs.macromol.2c01017
Macromolecules 2022, 55, 9452−9464

during evaporation-induced self-assembly (EISA) in thin films. Swelling of the films lowers the glass transition temperatures of polymer blocks, allowing an increase in mobility.[16−19] Since BCP self-assembly is the process by which polymer chains spontaneously organize into specific morphologies according to enthalpic and entropic driving forces, higher polymer chain mobility accelerates periodically ordered mesostructure formation, which otherwise may become trapped in non-equilibrium or metastable structures and phases. Moreover, SVA can help BCP systems reach a neutral free surface to minimize surface-energy-based preferentiality of particular blocks, which is an important factor determining mesostructural orientation.[4] Though thermal annealing is a method regularly used to reach thermodynamic equilibrium in the bulk, SVA is more regularly used for BCP thin films and proves advantageous in its viability in systems with blocks of dissimilar surface tensions or those containing blocks vulnerable to thermal degradation.[20] Another important consideration for thin film morphology is the choice of solvent, as different solvents may have contrasting block selectivity.[16−19,21−27] Careful optimization of thin film preparation can therefore be a complicated process that requires thoughtful experimental design to achieve a desired film morphology.

Advantages of operating within the thin film regime, as compared to bulk samples, include shorter self-assembly time scales and the potential for wide-ranging applications like membranes, organic−inorganic composites, photonic devices, and patterning templates.[10] Characterization of BCP thin film structure is therefore an important area of study. Common techniques for investigating BCP thin film morphology include grazing incidence small-angle X-ray scattering (GISAXS), scanning and transmission electron microscopies (SEM/TEM), and atomic force microscopy (AFM).[9,28] Combining analyses of these conventional techniques often provides a more comprehensive understanding of both film surface and substructure properties. Optical super-resolution microscopy (OSRM) is an emerging complementary imaging technique for BCP thin film structural characterization.[29] OSRM alleviates certain limitations of more traditional methods by providing noninvasive three-dimensional (3D) structural information as well as allowing *in situ* studies without the need for high vacuum or high-energy beams, which can damage sensitive organic materials.[30−33] As polymer compositions and structures grow more complex to meet the ever-evolving demand for new and specific material properties, it becomes all the more important to comprehensively characterize these systems with complementary tools like OSRM.[34,35]

OSRM overcomes Abbe's diffraction limit of visible light, which has restricted the resolution of optical microscopes to ∼200 nm for well over a century.[36] While finding rapid and extensive use in the biological sciences, it has only gradually made its way into the polymer community despite its vast potential. OSRM techniques developed for aqueous environments have been applied to polymer science, yielding such insightful capabilities as 3D mapping of crosslink heterogeneities for individual colloidal gel particles.[37] Recent studies have suggested that a subset of OSRM termed single-molecule localization microscopy (SMLM) may be optimized for more polymer-relevant environments, as in the case of resolving single polymer chains in the condensed state.[38] One popular SMLM technique is stochastic optical reconstruction microscopy (STORM).[39] STORM uses photoswitchable fluorophores to achieve on−off blinking between fluorescent and dark states that enables localization of densely populated optical emitters and reconstruction of super-resolved images.[33] With photoswitchable probes exhibiting the appropriate blinking statistics being a critical requirement for STORM emitters, the development of such probes that also selectively associate with desired polymer environments (*e.g.*, particular BCP blocks) emerges as a necessary step in the adaptation of OSRM to polymer science. As such, the soft matter community stands to reap great benefits from the advancement of polymer-selective OSRM probes.[33]

The present study centers on the topic of BCP thin film self-assembly and morphology characterization together with an exploration of an advanced OSRM probe labeling method for such polymer systems. Careful optimization of sample preparation, characterization, and analysis of poly(isoprene)-*block*-poly(styrene)-*block*-poly(*N*,*N*-dimethylaminoethyl methacrylate) (PI-*b*-PS-*b*-PDMAEMA or ISA) triblock terpolymer thin films is reported. Spin-coated films undergo SVA-induced self-assembly, with considerations for solvent choice and solution concentration. Surface visualization via AFM suggests a hexagonally ordered top surface structure. Fast Fourier transform (FFT) and Voronoi analyses are presented to provide additional quantitative assessment of AFM surface images. The combination of GISAXS and SEM cross-sectional data is consistent with a co-continuous gyroid morphology of the ISA thin films below the hexagonally ordered top surface layer. This observation is corroborated by etching of the top surface and subsequent SEM imaging of the substructure, revealing characteristic patterns expected from a co-continuous gyroidal structure.

With both known composition and this distinction between the top- and sub-surface networks, such a complex architecture provides a good model system to test the capabilities of OSRM on polymers at this scale. As such, STORM is finally used to expand the conventional characterization toolset to include OSRM. Multicomponent labeling of polymeric nanodomains is highly desirable for optical insights into soft matter, *e.g.*, revealing exchange pathways in dye-labeled supramolecular polymers.[40] Such examples of multicolor labeling of polymers, however, are primarily limited to studies using reactive chemistries to pre-tag monomers and/or label polymers during or after polymerization with biologically relevant fluorophores. We previously demonstrated covalent polymer−nanoprobe attachment strategies to label one reactive domain of polystyrene-*block*-poly[(allyl glycidyl ether)-*co*-(ethylene oxide)] (PS-*b*-P(AGE-*co*-EO) diblock copolymers post-assembly using click chemistries for one- or two-color STORM imaging.[41,42] Rather than covalent labeling, incorporation of two orthogonal, ultrabright optical probes—fluorescent-dye-encapsulating aluminosilicate Cornell prime dots referred to as aC' dots—into the BCP thin films is achieved via facile physical mixing into the ISA solution before spin-coating and subsequent self-assembly. Due to their polar poly(ethylene glycol) (PEG) surface ligands, PEGylated aluminosilicate core−PEG shell (core−shell) probes are expected to associate during self-assembly with the polar PDMAEMA block of the triblock terpolymer. In contrast, from earlier studies, PEGylated aC' dots further surface-modified with benzyl groups ("BaC' dots") are expected to associate with the PS block.[41] STORM imaging of the resulting nanocomposite thin film surfaces supports these hypotheses. In analogy to biological studies, the mixing of orthogonal, high-brightness, and high-photostability core−shell OSRM probes, which

https://doi.org/10.1021/acs.macromol.2c01017
Macromolecules 2022, 55, 9452−9464

associate with specific blocks of a BCP per their tunable surface chemical properties, provides a versatile toolbox for the multicolor OSRM characterization of BCP self-assembly-derived nanocomposite surface nanostructures in the far field of a conventional optical fluorescence microscope.

EXPERIMENTAL METHODS

Materials. Poly(isoprene)-*block*-poly(styrene)-*block*-poly(*N*,*N*-dimethylaminoethyl methacrylate) (PI-*b*-PS-*b*-PDMAEMA or ISA) was synthesized using anionic polymerization as previously reported.[43] PEGylated aluminosilicate nanoparticles (Cy3-aC' dots) were synthesized and subsequently characterized with fluorescence correlation spectroscopy (FCS) employing previously published methods.[44] Benzyl-group-modified/PEGylated aluminosilicate nanoparticles were synthesized and subsequently characterized with various techniques, including FCS, as described elsewhere.[41] Double-polished <100> silicon wafers were purchased from WRS Materials. The cover glass and ruthenium tetroxide were purchased from Electron Microscopy Sciences. Deuterated chloroform was purchased from Cambridge Isotope Laboratories, Inc. Toluene was purchased from Alfa Aesar. Ethanol was purchased from VWR International. Cy3- and Cy5-maleimide dyes were purchased from Lumiprobe Corp. All other chemicals were purchased from Sigma-Aldrich. Chemicals were used as received.

Polymer Characterization. The ISA triblock terpolymer was synthesized via anionic polymerization[43] and characterized with a combination of gel permeation chromatography (GPC) and proton nuclear magnetic resonance (^{1}H NMR) spectroscopy. For GPC (see Figure S1), the synthesized triblock terpolymer was dissolved in tetrahydrofuran (THF) to form a solution of ∼1−2 mg/mL and run at 30 °C through a single column equipped with a refractive index detector and a UV detector. For ^{1}H NMR spectroscopy characterization, the PI-*b*-PS-*b*-PDMAEMA was dissolved in deuterated chloroform to form a dilute solution. ^{1}H NMR spectroscopy data (see Figure S2) were collected on a Mercury 300 MHz spectrometer using a standard probe of ^{1}H/X and processed with Mestrelab Mnova for signal integration. The triblock terpolymer had a molar mass of M_n = 85.0 kg/mol, a polydispersity of 1.28, and PI/PS/PDMAEMA weight fractions of 0.18:0.36:0.46, with around 5% of the PI attributed to 1,2- or 3,4-addition (Figure S2). Given the composition and molar mass, the polymer is hereafter designated as ISA_{85}.

Particle Characterization. Functional aluminosilicate core−organic ligand shell (core−shell) aC' dots and BaC' dots were synthesized as previously reported.[41,44] In this work, the aC' dot encapsulates Cy3 dye and is stabilized by an organic shell composed solely of PEG-silanes (see Scheme S1a), while the BaC' dot encapsulates Cy5 dye and is stabilized by a combination of PEG- and benzyl-silanes (see Scheme S1b). As-synthesized particles were up-concentrated using GE Healthcare Vivaspin MWCO 30 kDa centrifuge spin filters before two runs through a GPC column with Sephacryl S-300 High Resolution resin (GE Healthcare) using a 0.9 wt % NaCl aqueous solution (see Figure S3a). Particles were subjected to optical characterization in the form of FCS (see Figure S3b,c) and UV−vis absorbance (see Figure S3d,e) to determine the average hydrodynamic diameter and dyes per particle, respectively.

Polymer and Polymer Nanocomposite Thin Film Assembly and Etching. ISA_{85} was freeze-dried by dissolution in 1,4-dioxane for 1 h before immersing the polymer-solution-containing round-bottom flask in liquid nitrogen. The flask was next connected onto a Schlenk line to dry at room temperature for 24 h. The freeze-dried ISA_{85} was then dissolved in THF for 3 h to form 1.5 wt % or 5 wt % solutions, distributed into Teflon-top sample storage vials, and stored in the freezer until use. The polymer solution was removed from the freezer as needed and brought to room temperature prior to spin-coating. Immediately before spin-coating, silicon wafers were cut into 1 cm^2 squares and then sonicated in acetone and isopropanol, respectively, for 15 min each. The wafers were subsequently rinsed with isopropanol, dried under nitrogen flow, and baked at 110 °C for 10 min. The preparation steps to generate self-assembled thin film samples are schematically shown in Scheme S2. The polymer solution (∼0.2 mL) was deposited to completely cover the surface of a cleaned wafer and spin-coated for 1 min at 3000 RPM with an acceleration of 600 RPM/s. Spin-coated thin films were subsequently submitted to solvent vapor annealing (SVA) in a THF-vapor-saturated atmosphere at room temperature for 19 h. For thin films prepared with toluene, THF was substituted by toluene for both polymer dissolution and SVA, and annealing time was increased to 120 h.

For scanning electron microscopy (SEM) imaging of the top surface, thin films were subjected to an etching step. To that end, the as-made thin films were cut into 0.25 cm^2 squares with a diamond-tipped scriber and etched via reactive ion etching (RIE) with an Oxford PlasmaLab 80+ etcher using CF_4 plasma for 7 s at a forward power of 150 W with a CF_4 flow rate of 30 sccm and a pressure of 40 mTorr.

Nanocomposite thin films were generated from ISA_{85} containing optical nanoparticle probes in the form of Cy3-dye-encapsulating aluminosilicate core−poly(ethylene glycol) (PEG) shell (core−shell) Cornell prime dots ("Cy3-aC' dots", see Scheme S1a), PS-compatible benzylated aC' dots encapsulating Cy5 dye ("Cy5-BaC' dots", see Scheme S1b), or both (*i.e.*, Cy3-aC' dots and Cy5-BaC' dots together) for single-color or two-color stochastic optical reconstruction microscopy (STORM) imaging, respectively. These nanocomposite thin films were generated in the following way: Cy3-aC' dots and/or Cy5-BaC' dots were added to a 5 wt % solution of ISA_{85} in THF at probe concentrations of either 430 nM or 150 nM and stirred for 1 h prior to spin-coating. Using FCS-derived particle diameters and assuming an effective density of 2.0 g/cm^3,[45] these concentrations correspond respectively to ∼0.06 wt % (Cy3-aC' dots) or ∼0.02 wt % (Cy3-aC' dots)/∼0.04 wt % (Cy5-BaC' dots) relative to the ISA_{85} in the solution. For two-dot nanocomposite thin films, both Cy3-aC' dots and Cy5-BaC' dots were added in this manner such that the individual dot concentration in the solution was 150 nM each. Immediately prior to spin-coating, silicon wafers were cut and cleaned as described above, while pieces of cover glass—an alternative thin film substrate—were sonicated in ethanol for 15 min, dried under nitrogen flow, and baked at 110 °C for 10 min. Nanocomposite thin films were then spin-coated and solvent annealed according to the protocol outlined above. All neat and nanocomposite thin films used for comparative purposes herein were prepared from the same stock ISA_{85}/THF solution, at the same time, and under the same conditions.

Structural Characterization and Analysis. As delineated below, top surface structures of the self-assembled thin films were first studied by AFM; the resulting images were subjected to fast Fourier transform (FFT) and Voronoi analyses. Cylinder-to-cylinder (PI core to adjacent PI core) distances and standard deviations thereof were calculated based on 20 cylinder pairs in ImageJ randomly selected over various regions. Subsurface structures were then investigated by a combination of grazing-incidence small-angle X-ray scattering (GISAXS), SEM of film cross-sections, and SEM of etched film surfaces. Finally, AFM results of the top surface structures were compared with those from stochastic optical reconstruction microscopy (STORM).

AFM data were obtained utilizing a Digital Instruments Multimode scanning-probe microscope. Samples were characterized using monolithic silicon noncontact high resonance frequency AFM tips purchased from NanoWorld with a force constant between 21 N/m and 78 N/m under tapping mode. All images were collected at a resolution of 512 × 512 pixels and at a scan rate of 1.2 Hz.

For FFT, AFM images first went through a contrast increase in ImageJ. For consistency, the display window extrema were set in the contrast menu such that pixel values under 42 were displayed as black and pixel values above 212 were displayed as white (*i.e.*, giving a display range of 170 pixels); the images were then rendered binary. Since the hexagonal patterns were not perfectly symmetric, wedge integrations were subsequently used around the elongated axis of the two-dimensional (2D) FFT to generate one-dimensional (1D) plots, from which center-to-center cylinder distances of the hexagonal patterns were deduced. For Voronoi analysis, the same AFM image

https://doi.org/10.1021/acs.macromol.2c01017
Macromolecules 2022, 55, 9452−9464

was processed using the Split Channels function in ImageJ into separate red-, blue-, and green-channel grayscale images (see Figure S4). With the greatest contrast of the three, the green channel was rendered binary to generate a Voronoi figure displaying the packing structure, from which the distribution of next-nearest neighbors was calculated. First, substructures falsely identified by the software from contrast variations in the grayscale images at PS−PDMAEMA interfaces were eliminated by setting the "minimum particle size" in ImageJ such that features <900 nm^2 in size were excluded (see Figure S5). This lower bound (900 nm^2) was selected based on visual inspection of the AFM images, which showed no periodic features of interest below this size. Next, subunits along the edges of the images that introduced artificial defects were excluded by selecting the Exclude on Edges function.

Thin film GISAXS data were obtained at the Soft Matter Interfaces beamline (12-ID) of the National Synchrotron Light Source II at Brookhaven National Laboratory. Data were collected with a 14 keV beam at a sample-to-detector distance of 497 cm and incident angles between 0.10° and 0.15°. 2D GISAXS data were processed and plotted using the MATLAB-based software GIXSGUI (version 1.7.1) with the distorted wave Born approximation theory.

To prepare SEM samples, cleaved or etched ISA_{85} thin films were stained with RuO_4 vapor for 10−20 min. Images were collected using a Zeiss Gemini 500 SEM with an in-lens detector at an accelerating voltage of 2 keV. A working distance of 1.9 mm was employed for film cross-section imaging and 4.5−5.5 mm for etched surface imaging of uncoated samples.

Optical Super-Resolution Imaging. Nanocomposite thin film samples were immersed in deionized (DI) water, face-down onto a circular glass cover slip held in place by a steel imaging well located above a 1.45 NA 100× objective. A schematic representation of this setup[42] is displayed in Figure S6. Data were collected in a total internal reflection fluorescence (TIRF) microscope geometry. The Cy3-aC' dots were excited by a 561 nm laser and Cy5-BaC' dots by a 640 nm laser; fluorescence signal was spectrally filtered using a 561 nm band-pass filter (Cy3) or a 640 nm band-pass filter (Cy5), respectively, and recorded with an Andor iXon EMCCD camera. A series of 10,000 frames with a time resolution of 30 ms/frame were acquired for each sample. For two-color STORM images, a specific thin film region was exposed first to only the 640 nm laser, and data were collected from the Cy5-BaC' dot fluorescent activity over that area; the same region was then exposed to only the 561 nm laser, and data were collected from the Cy3-aC' dot fluorescent activity. Reconstructed super-resolution STORM images were generated using the ImageJ plugin ThunderSTORM.[46] Data sets for the same region of nanocomposite ISA_{85} thin films containing both Cy3-aC' dots and Cy5-BaC' dots were reconstructed individually into single-color images and then overlain to produce a two-color STORM image of the single region. The sample, imaging setup, plane of focus, and area of observation remained unchanged between data collections over the same area. As with AFM, cylinder-to-cylinder distances—non-fluorescent PI core to adjacent PI core, surrounded by green signal from the Cy3-aC' dots in the PDMAEMA matrix domain—and standard deviations thereof were calculated based on 20 cylinder pairs in ImageJ randomly selected over various regions.

RESULTS AND DISCUSSION

Thin Film Optimization and Structural Analysis. This work employed an 85 kg/mol poly(isoprene)-*block*-poly(styrene)-*block*-poly(*N*,*N*-dimethylaminoethyl methacrylate) (PI-*b*-PS-*b*-PDMAEMA) triblock terpolymer, with PI/PS/PDMAEMA weight fractions of 0.18:0.36:0.46, termed ISA_{85}. Different preparation conditions were explored to generate ISA_{85} thin films with well-ordered surface structures, as shown by means of atomic force microscopy (AFM) in Figure 1. It was first concluded that solvent vapor annealing (SVA) was a critical step to enable the formation of nanostructured surfaces: Spin-coated films that did not undergo SVA showed no identifiable surface patterns in AFM (Figure 1a), while hexagonally packed structures appeared after annealing the films in tetrahydrofuran (THF) vapor for 19 h (Figure 1b).

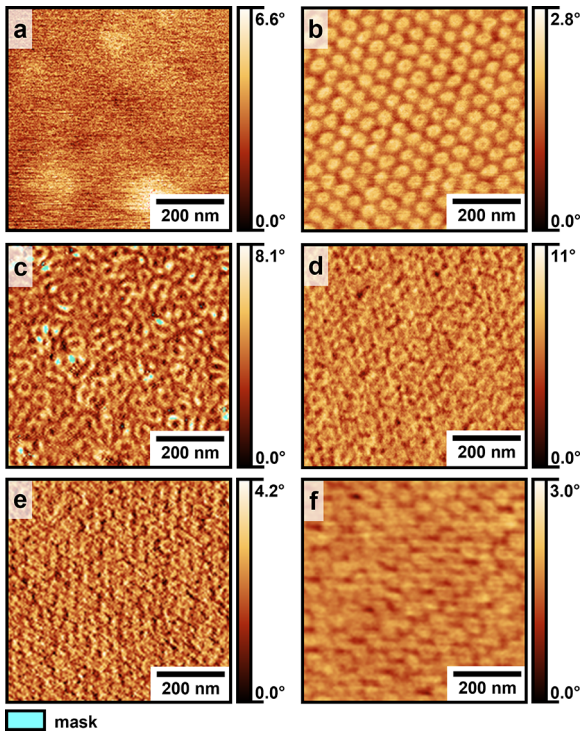

Figure 1. AFM phase images of ISA_{85} thin film surfaces revealing the effect of (a, b) SVA, (c, d) solvent, and (e, f) solution concentration. Shown are top surface morphologies of films annealed in THF for (a) 0 and (b) 19 h, dissolved in and solvent-annealed with (c) toluene for 120 h or (d) THF for 19 h, and prepared from (e) 1.5 and (f) 5 wt % THF solutions.

Solvent selection is also important in determining top surface structure and allowing rapid ordering by increasing polymer chain mobility.[16,21] While previous studies identified toluene as a suitable solvent for self-assembly of relatively thick PI-*b*-PS-*b*-PDMAEMA composite films,[47] it was found to be less optimal for the formation of well-ordered, self-assembled thin films. Spin-coated films prepared from ISA_{85} dissolved in toluene took 120 h to form a distinguishable surface structure when annealed in toluene (Figure 1c). Conversely, those prepared in THF required only 19 h of SVA (Figure 1d). The concentration of the polymer solution also played a key role in defining the surface structure: A higher concentration led to thicker films and better-defined surface structures. Increasing polymer concentration in THF from 1.5 wt % (Figure 1e) to 5 wt % (Figure 1f) yielded a superior surface structure, which was accompanied by a film thickness increase from around 100 nm to above 300 nm, as estimated by AFM.

From these initial studies, in the following experiments, optimized nanostructured ISA_{85} thin films were reproducibly prepared by spin-coating a 5 wt % THF solution onto a silicon wafer followed by SVA in THF for 19 h. Resulting films had a thickness of ∼330 nm. Figure 2a,b shows the top surface morphology, as imaged with AFM. Films displayed periodically ordered hexagonal patterns with distinct regions attributed by relative composition to each of the three blocks: PI−PS core−shell cylinders in a majority PDMAEMA matrix. Figure 2c,d depicts this structure schematically, with PI cylinder cores

https://doi.org/10.1021/acs.macromol.2c01017
Macromolecules 2022, 55, 9452−9464

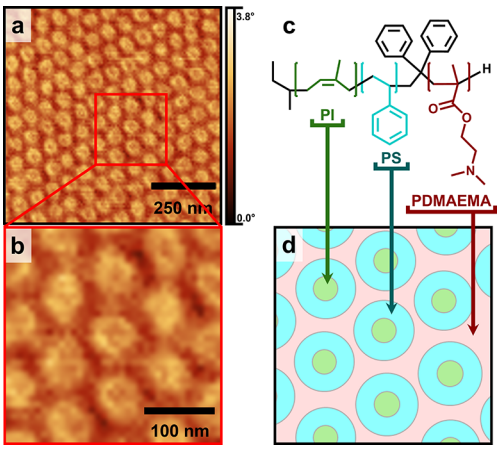

Figure 2. (a) Representative AFM phase image of an ISA_{85} thin film. A magnified region marked with a red square in (a) is shown in (b), enabling identification of all three top surface blocks of the ISA_{85} structure depicted in (c). A schematic of the top surface morphology consistent with the AFM images is depicted in (d), showing PI cylinder cores (green), PS cylinder shells (blue), and the PDMAEMA matrix (light pink).

represented in green, PS cylinder shells in blue, and the PDMAEMA matrix in light pink.

AFM images of ISA_{85} thin film surface morphology (Figure 3a) were further subjected (Figure 3b,c) to fast Fourier transform (FFT) and Voronoi analyses for a more quantitative assessment of the top surface structure (Figure 3b,c). Consistent with AFM, FFT analysis (Figure 3d) suggests a slightly distorted hexagonal lattice with a center-to-center distance of cylinders of 72.8 nm (based on the long axis of the

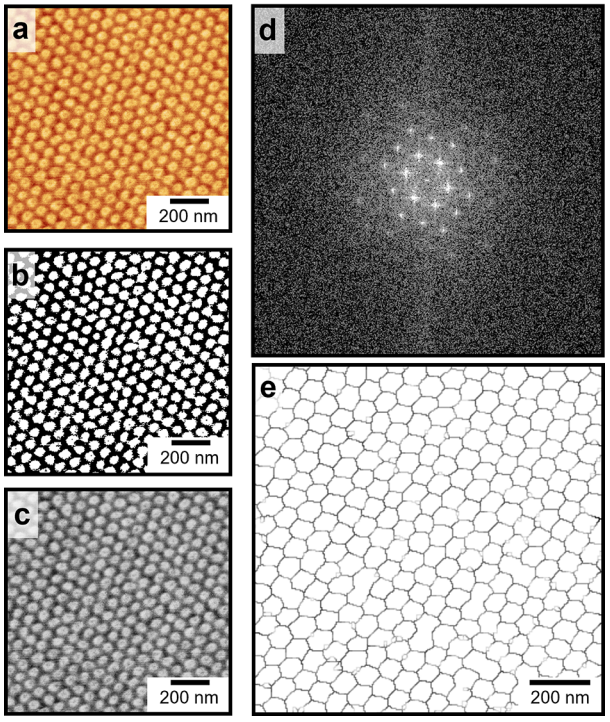

Figure 3. (a) Processing of ISA_{85} thin film surface AFM phase image. (b) Increasing contrast and rendering the AFM image binary or (c) splitting the AFM image into monochromatic channels enabled (d) FFT and (e) Voronoi analyses.

distorted structure). Voronoi image analysis (Figure 3e) visually confirmed that the vast majority of structural subunits—here, the cylinders—had six nearest neighbors, as expected from a hexagonal structure. Excluding artifacts from poor contrast and image edges (see Experimental Methods), the fraction of subunits having six nearest neighbors was 94.6%, whereas fractions with five, seven, and eight nearest neighbors were, respectively, only 3.4%, 0.3%, and 1.7%. Both FFT and Voronoi analyses helped to corroborate the high degree of periodic ordering of the ISA_{85} thin film surface.

Following these analyses, which provided insights into the top surface morphology, grazing-incidence small-angle X-ray scattering (GISAXS) was performed to better understand the subsurface structure of the ISA_{85} thin films. The observed scattering pattern (Figure 4a) was analyzed with a MATLAB-based code and determined to be consistent with a core−shell double gyroid structure with the (211) planes parallel to the substrate and compressed 52% along [211], *i.e.,* along the film normal. The associated lattice parameters were as follows: a = 90.7 nm and $b = c$ = 121.4 nm, with angles $\alpha = 98°$ and $\beta = \gamma = 113°$. According to the lattice parameters, the distance between neighboring (211) planes is 25.5 nm. Compression of the film was likely a result of rapid drying that occurred immediately upon the removal of samples from the SVA environment, consistent with earlier studies of such thin film structures.[48−51]

For thin film cross-sectional analysis, ISA_{85} thin films were cleaved and cross-sections were stained with RuO_4 for scanning electron microscopy (SEM). The resulting images (Figure 5) showed periodically ordered structures throughout the "bulk" of the thin film with a measured distance of approximately 23.8 nm between layers, close to the calculated plane-to-plane value (25.5 nm) from the GISAXS analysis (vide supra).

While AFM identified a hexagonally ordered top surface morphology, GISAXS analysis probes the thin film substructure, which were consistent with a double gyroid morphology. To account for these structural differences, it was of interest to investigate the change in structure when moving away from the top surface layer, *i.e.,* deeper into the film. To visualize this transition, ISA_{85} thin films were etched with CF_4 plasma and subsequently imaged with SEM. Experiments with alternative plasmas had revealed CF_4 to be the optimal choice: Using an O_2 plasma resulted in selective etching and surface damage, whereas argon plasma proved too weak to effectively etch away the top surface. Films etched with CF_4 plasma were subsequently stained with RuO_4 for ∼15 min to increase SEM image contrast.

Figure 6a shows an SEM image of an ISA_{85} film etched for 7 s. While there are still regions displaying hexagonal order, the image of the etched film now also clearly reveals areas that resemble a co-continuous structure. Regions with hexagonal lattice structure had a center-to-center cylinder distance of 71.2 ± 1.6 nm, close to the 72.8 nm value obtained from FFT analysis of the top surface structure (vide supra). The spacing between the neighboring repetitive features in the (211) plane (see red double arrow in Figure 6d) was 117.0 ± 4.1 nm, similar to the 112.7 nm spacing calculated from GISAXS data. Figure 6b shows an enlarged SEM image area that displays features consistent with a co-continuous structure. By comparing this pattern to MATLAB simulations of (211) planes of the double gyroid along the [211] axis at different depths (Figure 6c), a bent-triangular structure alternating from one side to another is clearly recognizable (see the blue box in

https://doi.org/10.1021/acs.macromol.2c01017
Macromolecules 2022, 55, 9452−9464

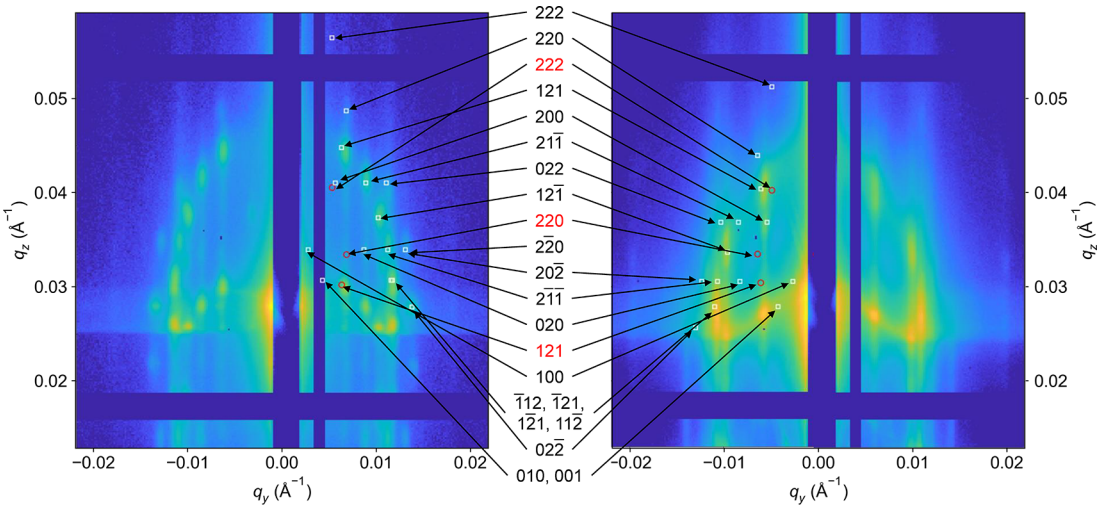

Figure 4. GISAXS patterns of (a) an ISA_{85} thin film and (b) an ISA_{85} + Cy3-aC' dot nanocomposite thin film showing indexed peaks matching a double gyroid structure with the (211) plane parallel to the surface and compressed along the film normal. White squares and red circles correspond to expected peak positions through the reflection and transmission channels, respectively, in GISAXS.

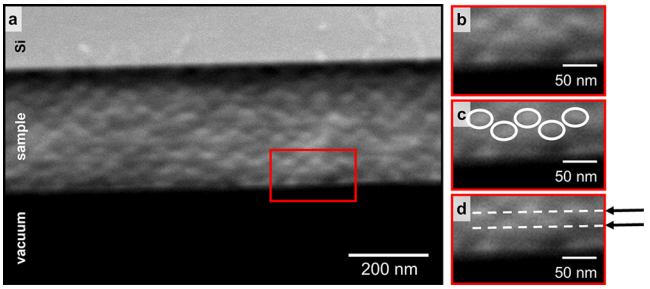

Figure 5. (a) Cross-sectional SEM image of an ISA_{85} thin film revealing a periodically ordered subsurface structure. The area outlined with a red box is enlarged in (b–d). White ovals in (c) indicate positions of periodic features for two neighboring planes in (b), which are represented with white dashed lines identified by black arrows in (d) and separated by about 24 nm.

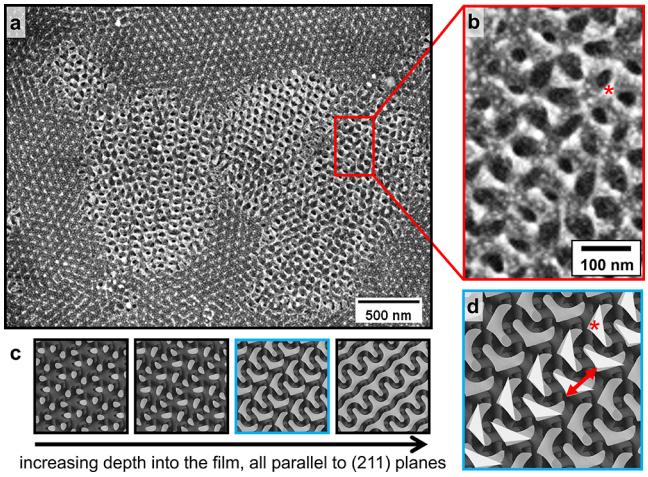

Figure 6. (a) SEM image with a selected area at higher magnification in the (b) red box of an ISA_{85} thin film surface after etching with CF_4 plasma for 7 s and (c) simulated (211) plane morphologies of the co-continuous double gyroid along the [211] axis at different depths. Comparing (d) a specific slice, outlined in blue, from the simulation stack to the area enlarged in (c) reveals clear similarities. Red asterisks in (b) and (d) indicate PI-rich locations that appear brighter in SEM due to preferential staining of the PI block with RuO_4. The red double arrow in (d) indicates the spacing between neighboring repetitive features in the (211) plane.

Figure 6c). With the PI block stained more heavily as compared to PS, the corner marked with a red asterisk indicates a PI-rich location. These areas appear brighter in the SEM image from greater electron scattering and can be assigned to a similar structure in the simulation (compare Figure 6b,d).

Together, these results suggest a transition from a hexagonal top surface structure to a double gyroid morphology in the thin film substructure. This behavior is likely driven by surface energy effects associated with the polymer–air interface. Furthermore, this behavior is similar to a transition from a hexagonally perforated layer structure to a gyroid structure, which was previously observed in BCP thin films thermally annealed at different temperatures.[52] SEM cross-sectional imaging (see Figure S7) indicates that thin films were reduced to ∼270 nm in thickness upon etching. Comparison to their original thickness (∼330 nm, vide supra) suggests a top surface layer thickness of ∼60 nm.

The reproducible co-continuous structure makes ISA_{85} an especially appealing candidate for optical super-resolution microscopy (OSRM): Its hexagonally packed core–shell cylinder top surface layer makes for an interesting subject of study using high-lateral-resolution OSRM tools like single-molecule localization microscopies (SMLMs), while its gyroid substructure could be evaluated using coordinate-targeted OSRM tools with high axial localization accuracy, such as stimulated emission depletion microscopy (STED), in future studies.[33] Moreover, both of these mutually unique structures have here been well investigated using conventional polymer characterization techniques, encouraging as a next step expansion to OSRM imaging of the top surface. To that end, we adapted this system with tailored optical nanoprobes for surface imaging of thin film nanocomposites using SMLM in the form of stochastic optical reconstruction microscopy (STORM).

Optical Super-Resolution Microscopy Imaging. For the application of OSRM imaging in polymer science, exploration of methods to incorporate optical probes into

https://doi.org/10.1021/acs.macromol.2c01017
Macromolecules 2022, 55, 9452–9464

polymers is of increasing interest.[33] Previous work[42] showed successful attachment of dye-encapsulating core−shell silica nanoparticles via various click chemistries to one domain within a diblock copolymer thin film surface for STORM. Subsequent experiments demonstrated selective incorporation of similar nanoparticle probes with nonpolar surface ligands into the nonpolar PS block of the same BCP and their characterization with STORM.[41] Here, PEGylated aluminosilicate nanoparticles termed aC' dots synthesized as previously reported,[44] with polar PEG surface ligands and encapsulating Cy3 dye, were used to passively label the polar PDMAEMA block of the ISA_{85} to enable STORM imaging (Scheme S1). Dye-encapsulating aC' dots show substantial brightness as well as photostability enhancements over their corresponding free dyes; the fourfold-coordinated aluminum in the aluminosilicate core is further responsible for optical dye blinking, likely via photoinduced redox processes, allowing STORM imaging that requires only one excitation laser (rather than two) and no specific imaging cocktails (*e.g.*, including toxic β-mercaptoethanol or oxygen scavengers).[44] They therefore present an attractive alternative to regular dye-based labeling approaches to provide the required optical blinking over extended periods of time. At the same time, their nature allows simultaneous assessment of BCP self-assembly-based nanocomposites, an important field of polymer science in its own right.[53]

Nanoparticle incorporation was achieved by simply adding Cy3-aC' dots to the stirring ISA_{85}−THF solution before spin-coating and co-assembly, taking advantage of the affinity of the purely PEGylated dots to the polar PDMAEMA block. PDMAEMA is widely used as a polar/hydrophilic segment in BCPs,[54−57] while PEG is a polar/hydrophilic polymer often used to provide water solubility to hydrophobic drugs and proteins.[58,59] Considering the polar character of both PEGylated aC' dot surface ligands and the PDMAEMA block of ISA_{85}, the nanoparticles should favor this block after solution mixing and subsequent evaporation-induced self-assembly (EISA). Besides enthalpic favorability, incorporation into the PDMAEMA block is also consistent with conformational entropy considerations. The hydrodynamic diameter of the Cy3-aC' dots was ∼4.4 nm, as calculated from fluorescence correlation spectroscopy (FCS), which was slightly smaller than the ∼4.7 nm radius of gyration for PDMAEMA, approximated using the freely jointed chain model and Kuhn length of poly(methyl methacrylate).[60] The relatively smaller size of the particles helps to prevent segregation driven by conformational entropy loss when PDMAEMA chains wrap around the nanoparticles.[61]

After nanocomposite thin film self-assembly via the optimized protocol (see Experimental Methods), it was first confirmed that surface structures of thin films prepared with and without Cy3-aC' dots showed the same characteristic, periodically ordered hexagonal patterns discussed previously (compare Figure S8a,b). Successful incorporation of Cy3-aC' dots into the thin film was suggested through the expansion of the observed hexagonal center-to-center cylinder spacing relative to that of the neat ISA_{85} film. For thin films prepared under otherwise identical conditions and at the same time, neat ISA_{85} films (without Cy3-aC' dots) showed an average center-to-center spacing of 73.3 ± 1.9 nm in AFM, while those prepared with Cy3-aC' dots exhibited a larger spacing of approximately 81.2 ± 2.0 nm, an increase of 10.8%. Such an increase in center-to-center distance suggests that the nanoparticles are successfully incorporated into the ISA_{85} thin film and is consistent with the swelling of the PDMAEMA matrix volume by Cy3-aC' dots. In parallel, GISAXS was performed on the nanocomposite film to investigate the evolution of the substructure. The GISAXS pattern can again be fitted with the gyroidal structure, having the same degree of compression along the film normal, with a = 96.1 nm, $b = c$ = 128.7 nm, and angles α = 98° and $\beta = \gamma$ = 113° (Figure 4b). The smaller increase in lattice dimensions of 6.0% revealed by GISAXS could be attributed to the slight preference of the Cy3-aC' dots to be on the surface, thus swelling surface morphology (probed by AFM) more than the "bulk" film substructure (probed by GISAXS). Combining results from AFM and GISAXS, incorporation of OSRM probes preserved the mesostructural integrity of the top surface as well as the substructure (*i.e.*, pure ISA_{85} and nanocomposite thin films exhibited the same morphology). However, we must also highlight the dual functionality of aC' dots as both STORM probes and inorganic nanoparticle additives, the latter of which are frequently used as structural agents to modify polymer morphology; composition; and mechanical, thermal, and electrical properties.[62] It is important to note the significance of polymer structural manipulation through or even during the self-assembly process,[63] which has often been accomplished via incorporation of both organic[64,65] and inorganic[66,67] content. Tuning characteristics in such polymer−nanoparticle composites to control the resulting morphology post-synthesis thus also serves as an exciting potential avenue of study, especially when coupled with OSRM, *e.g.,* to investigate nanocomposite self-assembly or polymer interactions with nanoparticles.

STORM was performed to corroborate that the nanoparticles were incorporated selectively into the PDMAEMA block rather than nonspecifically distributed throughout the nanocomposite thin film. To aid STORM data collection, switching to glass substrates would reduce aberrations associated with interactions between the laser and default silicon substrate. With thin film self-assembly heavily dependent on polymer−substrate interfacial energy,[4] it was necessary to confirm the consistency of the thin film structure across different substrates. Fortunately, likely due to the similarity between the native oxide layer on silicon substrates and glass surfaces, changing from silicon to a glass substrate did not substantially alter the thin film surface morphology. The periodically ordered, hexagonally packed cylinder top surface structure could clearly be identified for films prepared on both substrates under otherwise identical conditions on the same day (compare Figure S8b,c).

To increase the signal-to-noise ratio, STORM data were collected in a total internal reflection fluorescence (TIRF) microscope configuration.[68] While TIRF setups regularly achieve optical sectioning of ≤100 nm in the z-direction relative to the glass−water interface, high-aperture objectives like the one used here can reduce this axial sectioning even further to ∼75 nm.[69] Probe proximity to the film surface also enhances signal, as near-field interactions at the surface contribute to the fluorescence detectable by such objectives.[68] Coupled with the ∼60 nm top surface layer thickness (vide supra) and the layer of water of indeterminate thickness between the film and glass surfaces, this generalization indicates that the greatest signal will indeed be primarily localized to the surface (*i.e.*, hexagonally packed core−shell cylinder) layer of the film rather than from the gyroidal substructure. Potential background noise from deeper film regions is further reduced upon image processing with

https://doi.org/10.1021/acs.macromol.2c01017
Macromolecules 2022, 55, 9452−9464

ThunderSTORM.[46] Furthermore, we have previously provided strong evidence of surface-selective imaging on nanostructured BCP surfaces on thinner films using the same choice of microscope configuration.[41,42] In all, we anticipate that the STORM imaging is therefore largely confined to the surface layer and that the signal from any probes incorporated into the substructure is negligible.

Optical data for nanocomposite thin films prepared with [Cy3-aC' dots] = 430 nM in the ISA_{85}/THF solution were reconstructed into false-color STORM images and compared to AFM surface images of the same films, as shown in Figure 7.

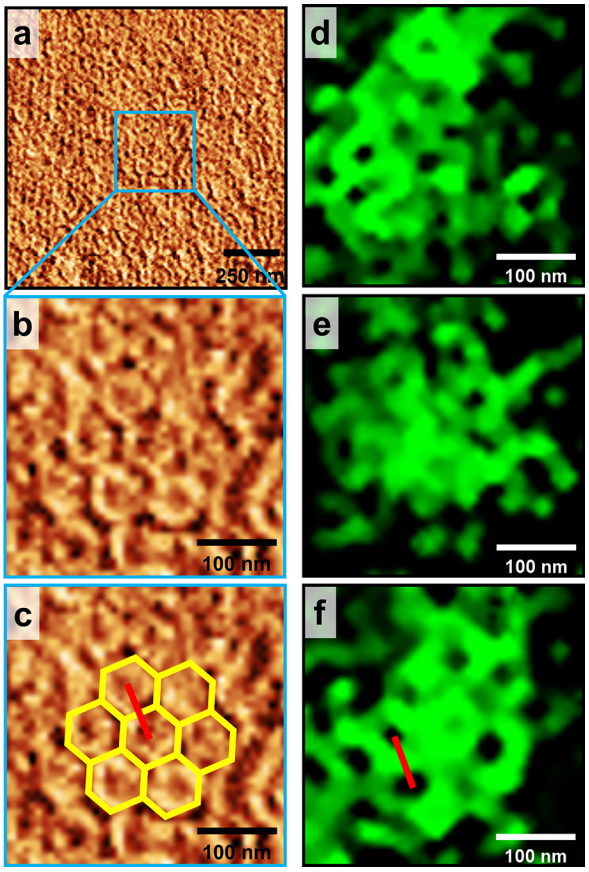

Figure 7. (a) AFM phase image of the top surface morphology of a nanocomposite film prepared from ISA_{85} and Cy3-aC' dots. The area within the blue box in (a) is enlarged in (b) and (c) to match the scale of a series of false-color STORM images in (d–f) of various regions from the same film. The yellow hexagon in (c) shows an example of hexagonal packing, and red lines in (c) and (f) demonstrate comparable cylinder-to-cylinder distance measurements in AFM and STORM, respectively.

In the OSRM images (see Figure 7d–f), the signal from Cy3-aC' dots from various regions of the film appears green, which manifests as approximate outlines of a hexagonal structure. The absence of signal in the centers of these regions is consistent with Cy3-aC' dots preferentially integrated into the PDMAEMA matrix block of the triblock terpolymer. This conclusion was corroborated by comparing the cylinder spacing from AFM, 83.1 ± 2.1 nm, to the green circles' center-to-center distance as determined by STORM, 81.6 ± 4.2 nm (compare Figure 7c,f).

In biology, specific labeling of different structures for OSRM is frequently achieved via genetically encoded fluorescent proteins, conjugation of small-molecule organic dyes, and/or direct fluorescent antibody labeling (*i.e.*, immunostaining) in aqueous environments, all of which heavily rely on well-studied, biology-specific interactions.[33,70] Conversely, labeling of nanoscopic structures in polymers for OSRM imaging has relied primarily on reactive chemical attachment or nonspecific association of fluorophores to single domains.[33,71] The often nanoscale features in polymeric systems necessitate bright, photostable, polymer-specific probes for structural visualization via OSRM. We have previously demonstrated passive/noncovalent and specific/covalent labeling of the PS and P(AGE-*co*-EO) nanodomains, respectively, in a polystyrene-*block*-poly[(allyl glycidyl ether)-*co*-(ethylene oxide)] (PS-*b*-P(AGE-*co*-EO) diblock copolymer with benzyl-modified PEGylated aC' dots, termed "BaC' dots" (mixing with PS domains), and PEGylated aC' dots carrying clickable groups (reacting with the exposed allyl groups of P(AGE-*co*-EO) domains on the thin film surface). Given the results represented in Figure 7 (*i.e.*, passive labeling of the PDMAEMA block with Cy3-aC' dots for STORM imaging), we hypothesized that multicolor labeling of different BCP nanodomains based solely on noncovalent affiliation of (B)aC' dot probes with chemically dissimilar blocks may be possible.

As proof-of-principle, nanocomposite thin films were prepared with either Cy3-aC' dots (~4.6 nm hydrodynamic diameter) or Cy5-BaC' dots (~6.0 nm hydrodynamic diameter) alone, or with both Cy3-aC' dots and Cy5-BaC' dots together (Scheme S1), and compared to a neat ISA_{85} thin film. While all films show morphologically similar top surface structures (*i.e.*, displaying a hexagonally packed core–shell cylinder structure; see Figure S9), differences in cylinder spacing consistent with incorporation of the dots into the ISA_{85} were identified. Data derived from AFM and STORM on average cylinder-to-cylinder distances, *d*, are compiled in Table 1. In experiments with only one type of particle, purely

Table 1. Comparison of STORM and AFM Cylinder-to-Cylinder Spacings (*d*)

film composition	*d* (nm)	
	AFM-derived	STORM-derived
ISA_{85}	72.9 ± 3.3	N/A
ISA_{85} + Cy3-aC' dots	81.0 ± 2.2	80.8 ± 3.8
ISA_{85} + Cy5-BaC' dots	77.3 ± 2.5	76.9 ± 4.0
ISA_{85} + Cy3-aC' dots + Cy5-BaC' dots	81.7 ± 2.4	81.3 ± 3.5

PEGylated Cy3-aC' dots appeared to incorporate into the PDMAEMA matrix of ISA_{85}, as already observed above and again suggested by the presence of fluorescence surrounding hexagonally packed black (*i.e.*, nonfluorescent) cores (see Figure S10a,c). The corresponding *d* spacing substantially increased by ~8 nm relative to the parent ISA_{85}, consistent with incorporation of aC' dot probes into the BCP matrix block[41] and corroborated by the STORM reconstructions. In experiments with only benzyl-group-functionalized/PEGylated Cy5-BaC' dots, fluorescence appeared around black circles and displayed hexagonal order, consistent with the closer proximity to the cylinder cores (see Figure S10b,c). Values of *d* for ISA_{85} thin films containing only Cy5-BaC' dots increased by only ~4 nm over the parent ISA_{85}; coupled with STORM, these results are consistent with the preferential association of these PS-compatible probes with the PS shells of the triblock terpolymer. In ISA_{85} thin films from mixtures with both Cy3-

https://doi.org/10.1021/acs.macromol.2c01017
Macromolecules 2022, 55, 9452–9464

aC' dots and Cy5-BaC' dots, the cylinder-to-cylinder distance increased by about 8−9 nm, the most of all samples studied (Table 1).

Figure 8 shows a two-color STORM image of a nanocomposite thin film prepared via physically mixing together in a "one-pot" approach both the purely PEGylated Cy3-aC' dots and the benzyl-group-functionalized/PEGylated Cy5-BaC' dots into the ISA_{85}/THF solution before spin-coating. From the difference in ligand shell polarity between these two probes and earlier experiments,[41] we hypothesized that these optical probes should preferentially associate with either the PDMAEMA matrix (Cy3-aC' dots) or the PS cylinder shells (Cy5-BaC' dots). In contrast, incorporation of either probe into the PI cylinder core was considered unlikely: In addition to chemical incompatibility, this block has the smallest radius of gyration of the three blocks (<4.2 nm), thereby favoring entropically driven demixing.[61] Meanwhile, the PS domain has the largest radius of gyration (>5.2 nm) to accommodate the slightly larger Cy5-BaC' dots. Indeed, we showed previously that a PS block with a radius of gyration similar to the hydrodynamic diameter of nonpolar BaC' dots will selectively incorporate these benzyl-modified probes while primarily excluding polar aC' dots.[41]

Corroboration of this hypothesis would manifest in STORM images in the form of a dominating Cy3-aC' dot signal (in false-color green) from the PDMAEMA matrix surrounding hexagonally packed circular regions, with a lesser Cy5-BaC' dot signal (in false-color red) from the cylinder shells closer to the nonfluorescent PI cores (appearing as black regions). These expectations were indeed met by two-color STORM experimental results. As Figure 8 demonstrates, sample regions could clearly be identified for which not only the Cy3-aC' dot and Cy5-BaC' dot signal intensities followed the expected behavior (*i.e.*, dominant behavior of green Cy3-aC' dot-based regions representing the PDMAEMA matrix), but signals from both probes also preferentially appeared in regions expected from the schematic of the surface morphology shown in Figure 2d, including examples of black regions representing the (undetected) PI core (via lack of fluorescence, see Figure 8d−f).

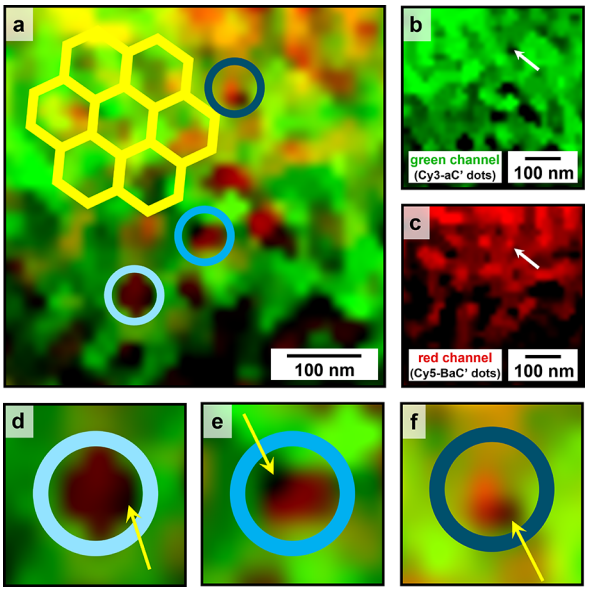

Figure 8. (a) Two-color STORM image of nanocomposite ISA_{85} thin films prepared with both Cy3-aC' dots and Cy5-BaC' dots, whose signals are shown respectively in the corresponding (b) green and (c) red channels. The yellow hexagon in (a) highlights an example of hexagonal packing. White arrows in (b) and (c) point to a black region (representing the PI domain) in a Cy3-aC' dot-based image in (b), which exhibits a smaller area of local heightened intensity in the corresponding Cy5-BaC' dot-based image in (c). Regions of interest denoted by blue circles in (a) are magnified in (d−f), with yellow arrows pointing to black areas without florescence in either channel, consistent with (unlabeled) regions of PI cylinder cores.

Inhomogeneous distribution of probes is anticipated in this nanocomposite system, where particle association of the two labels (*i.e.*, aC' dots and BaC' dots) is solely based on polar versus nonpolar interactions of the particle ligand shells with the different ISA_{85} blocks rather than specific, directed interactions, *e.g.*, leading to chemical bonding. However, as further shown in Figure 9, larger regions of the thin film top surface, as reflected by STORM imaging results, provide a consistent picture of the selective distribution of Cy3-aC' dot and Cy5-BaC' dot labels to different polymer nanodomains in the sample. Indeed, we were able to identify numerous examples of two-color STORM images showing color distributions consistent with the anticipated triblock terpolymer domains observed throughout the film (see a selection in Figure S11), while incorporation of the two kinds of optical probes preserved the surface morphology of the parent thin films (see Figure S9).

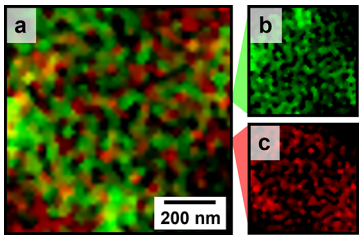

Figure 9. (a) Representative STORM image of two-dot nanocomposite ISA_{85} thin films, *i.e.*, prepared with both Cy3-aC' dots and Cy5-BaC' dots, whose individual signals in the (b) green and (c) red channels, respectively, are overlain to create (a). In the ISA_{85}/THF thin film preparation solution, [Cy3-aC' dots] = [Cy5-BaC' dots] = 150 nM.

It should be noted that while reactive/covalent labeling will inherently lead to a stronger probe−nanodomain association than relying on passive/physical interactions, the latter have been established as a viable tool for selective placement of nanoparticles within and/or around BCP blocks. Preferential wetting, often achieved, *e.g.*, through surface modification of nanoparticles with small-molecule ligands, has been shown to effectively compatibilize metal and metal oxide nanoparticles with specific nanodomains. An array of literature showcases how the careful design of nanoparticle surfaces exploits enthalpic and entropic favorability to modify spatial organization in such nanocomposites, *e.g.*, based on dipole−dipole and hydrogen bonding interactions.[61,66] Namely, tuning surface areal ligand density;[72] particle size and morphology, even in ternary blends;[61,73] and chemical composition[74,75] facilitates fine control over nanoparticle locations in BCP nanodomains. In addition, we have previously shown that covalent and noncovalent strategies may be used simultaneously and specifically for orthogonal labeling of different BCP nanodomains with block-specific nanoparticle probes for

https://doi.org/10.1021/acs.macromol.2c01017
Macromolecules 2022, 55, 9452−9464

STORM.[41] Results here suggest that sufficiently small probes with tunable surface chemistries can readily associate with polymeric nanodomains exhibiting compositional orthogonality (*e.g.*, polarity and/or molar mass differences). As such, in conjunction with reactive chemical attachment,[41,42,71] the design of effective probe labeling methods mediated via passive interactions serves to significantly expand the materials scientist's toolkit for specific multicolor labeling of polymers for OSRM imaging.

The OSRM work presented here makes use of high-brightness blinking and high-photostability STORM probes from encapsulated dyes in the particle cores with tunable surface chemistries in the ligand shells[76] that require only one laser and no imaging solution additives to generate OSRM images.[41,44] Taken together, these results demonstrate that polymer-specific optical probes can facilitate multicolor STORM imaging of nanostructured polymer surfaces via a facile physical solution mixing approach with the BCP, showcasing the potential of tunable probes to facilitate OSRM in synthetic polymers. Coupled with earlier results for two-color STORM imaging based on a combination of physical mixing and click-chemistry-based polymer association,[41] this work further expands the toolbox of available strategies using potent optical probes for OSRM-based nanostructure characterization in polymer science.

CONCLUSIONS

In this study, a series of structural characterization tools were applied to self-assembled ISA_{85} triblock terpolymer thin films. These techniques included thin film surface investigation enabled by atomic force microscopy (AFM), substructure analysis from grazing-incidence small-angle X-ray scattering (GISAXS), etched film surface and film cross-section visualization with scanning electron microscopy (SEM), and nanocomposite imaging via optical super-resolution microscopy (OSRM) in the form of stochastic optical reconstruction microscopy (STORM).

The comprehensive characterization of the ISA_{85} triblock terpolymer used here provides a systematic approach to developing and studying periodically ordered nanoscopic patterns in multicomponent block copolymer (BCP) thin films. In this work, all three nanodomains of the microphase-separated PI-*b*-PS-*b*-PDMAEMA are represented in the top surface layer, providing a model system for surface and substructure exploration. This desirable thin film surface structure, with hexagonally packed PI−PS core−shell cylinders in a PDMAEMA matrix, was achieved via spin-coating and solvent vapor annealing (SVA) from optimized choices of solvent, solution concentration, and SVA time. Fast Fourier transform (FFT) and Voronoi analyses of AFM images yielded quantitative information on the ordered surface patterns, while interpretation of GISAXS and SEM data provided insight into a structural transition from a hexagonal top surface structure to a co-continuous double gyroid morphology along the film normal into the thin film substructure.

Further work demonstrated a facile and effective solution mixing method to passively incorporate ultrabright STORM particle probes into the polar block of the ISA_{85}, enabling OSRM characterization of the top surface morphology of the resulting nanocomposite thin films. A comparison between AFM measurements and those derived from STORM on the same film clearly established that ultrasmall core−shell aluminosilicate nanoparticles (aC' dots) used as labels for STORM and with polar poly(ethylene glycol) (PEG) surface ligands are preferentially incorporated into the polar PDMAEMA matrix of the triblock terpolymer. This simple mixing approach of the two polar components in a common solvent thereby enables the use of STORM for surface nanostructure characterization, introducing a straightforward pathway to OSRM imaging of BCPs containing a hydrophilic block. Moreover, nanocomposite thin films prepared with PDMAEMA-compatible aC' dots and PS-compatible BaC' dots were consistent with the passive yet specific association of ultrabright optical probes with chemically distinct blocks. As with biological studies, this method facilitates multicolor OSRM characterization of BCP surface nanostructures by noncovalent physical mixing of probes with different "colors" (*i.e.*, encapsulated dyes) via tunable particle ligand surface chemistries and associated polarity into the specific blocks of a BCP.

ASSOCIATED CONTENT

Supporting Information

The Supporting Information is available free of charge at https://pubs.acs.org/doi/10.1021/acs.macromol.2c01017.

Additional experimental data and schematic illustrations: GPC and ^{1}H NMR characterization of ISA_{85}; particle characterization; Cy3-(B)aC' dot illustrations; ISA_{85} thin film preparation illustration; split-channel AFM images; Voronoi analysis exclusions; TIRF setup; SEM of etched ISA_{85} thin film cross-section; and AFM and STORM images of neat and nanocomposite ISA_{85} thin film surfaces (PDF)

AUTHOR INFORMATION

Corresponding Author

Ulrich B. Wiesner − *Department of Materials Science and Engineering and Kavli Institute at Cornell for Nanoscale Science, Cornell University, Ithaca, New York 14853, United States;* orcid.org/0000-0001-6934-3755; Email: ubw1@cornell.edu

Authors

Wennie Yun Lee − *Department of Materials Science and Engineering, Cornell University, Ithaca, New York 14853, United States;* Present Address: Formlabs Inc., Somerville, Massachusetts 02143, United States

Dana V. Chapman − *Department of Materials Science and Engineering, Cornell University, Ithaca, New York 14853, United States;* Present Address: Department of Biomedical Engineering, Yale University, New Haven, Connecticut 06511, United States; orcid.org/0000-0002-9605-1886

Fei Yu − *Department of Materials Science and Engineering and Department of Chemistry and Chemical Biology, Cornell University, Ithaca, New York 14853, United States;* orcid.org/0000-0002-8191-8096

William R. T. Tait − *Department of Materials Science and Engineering and Department of Chemical and Biomolecular Engineering, Cornell University, Ithaca, New York 14853, United States;* orcid.org/0000-0001-8932-9416

R. Paxton Thedford − *Department of Materials Science and Engineering and Department of Chemical and Biomolecular Engineering, Cornell University, Ithaca, New York 14853, United States;* Present Address: Formlabs Inc., Somerville,

Massachusetts 02143, United States; orcid.org/0000-0003-0811-227X

Guillaume Freychet − *National Synchrotron Light Source-II, Brookhaven National Laboratory, Upton, New York 11973, United States*

Mikhail Zhernenkov − *National Synchrotron Light Source-II, Brookhaven National Laboratory, Upton, New York 11973, United States;* orcid.org/0000-0003-3604-0672

Lara A. Estroff − *Department of Materials Science and Engineering and Kavli Institute at Cornell for Nanoscale Science, Cornell University, Ithaca, New York 14853, United States;* orcid.org/0000-0002-7658-1265

Complete contact information is available at: https://pubs.acs.org/10.1021/acs.macromol.2c01017

Author Contributions

†W.Y.L., D.V.C., and F.Y. contributed equally to this work. The manuscript was written through contributions of all authors, and all of the authors approved the final version of the manuscript.

Notes

The authors declare the following competing financial interest(s): U.B.W. and Cornell University have financial interest in Elucida Oncology, Inc., which licenses C dot intellectual property rights.

■ ACKNOWLEDGMENTS

The authors thank the U.S. Department of Energy (DOE), Office of Science, Basic Energy Sciences (DE-SC0010560), for funding this research. D.V.C. thanks the National Science Foundation (NSF) Graduate Research Fellowship Program (DGE-2139899) for support. This work made use of the Cornell Center for Materials Research (CCMR), supported by the NSF MRSEC program through Award DMR-1719875, and Cornell NanoScale Facility (CNF), supported by NSF Grant NNCI-2025233. It also used the Soft Matter Interfaces (SMI) beamline at the National Synchrotron Light Source II, a U.S. DOE Office of Science User Facility operated for the DOE Office of Science by Brookhaven National Laboratory under Contract DE-SC0012704.

■ REFERENCES

(1) Bates, F. S.; Fredrickson, G. H. Block Copolymers—Designer Soft Materials. *Phys. Today* **1999**, *52*, 32.

(2) Bates, F. S.; Fredrickson, G. H. Block Copolymer Thermodynamics: Theory and Experiment. *Annu. Rev. Phys. Chem.* **1990**, *41*, 525−557.

(3) Thomas, E. L.; Lescanec, R. L. Phase Morphology in Block Copolymer Systems. *Philos. Trans. R. Soc. London. Ser. A Phys. Eng. Sci.* **1686**, *1994*, 149−166.

(4) Segalman, R. A. Patterning with Block Copolymer Thin Films. *Mater. Sci. Eng. R Rep.* **2005**, *48*, 191−226.

(5) Floudas, G.; Vazaiou, B.; Schipper, F.; Ulrich, R.; Wiesner, U.; Iatrou, H.; Hadjichristidis, N. Poly(Ethylene Oxide-*b*-Isoprene) Diblock Copolymer Phase Diagram. *Macromolecules* **2001**, *34*, 2947−2957.

(6) Zheng, W.; Wang, Z. G. Morphology of ABC Triblock Copolymers. *Macromolecules* **1995**, *28*, 7215−7223.

(7) Lynd, N. A.; Meuler, A. J.; Hillmyer, M. A. Polydispersity and Block Copolymer Self-Assembly. *Prog. Polym. Sci.* **2008**, *33*, 875−893.

(8) Matsen, M. W. Self-Assembly of Block Copolymers in Thin Films. *Curr. Opin. Colloid Interface Sci.* **1998**, *3*, 40−47.

(9) Du, P.; Li, M.; Douki, K.; Li, X.; Garcia, C. B. W.; Jain, A.; Smilgies, D.-M.; Fetters, L. J.; Gruner, S. M.; Wiesner, U. B.; Ober, C. K. Additive-Driven Phase-Selective Chemistry in Block Copolymer Thin Films: The Convergence of Top−Down and Bottom−Up Approaches. *Adv. Mater.* **2004**, *16*, 953−957.

(10) Fasolka, M. J.; Mayes, A. M. Block Copolymer Thin Films: Physics and Applications. *Annu. Rev. Mater. Res.* **2001**, *31*, 323−355.

(11) Hückstädt, H.; Goldacker, T.; Göpfert, A.; Abetz, V. Core−Shell Double Gyroid Morphologies in ABC Triblock Copolymers with Different Chain Topologies. *Macromolecules* **2000**, *33*, 3757−3761.

(12) Gronski, W.; Stadler, R. Structural Regularity and Crystallization of Lithium Polyisoprene and Poly(Styrene-*b*-Isoprene-*b*-Styrene). *Polym. Bull.* **1980**, *2*, 289−395.

(13) Stadler, R.; Gronski, W. Effects of Phase Separation on Network and Viscoelastic Properties in SBS Thermoplastic Elastomers. *Colloid Polym. Sci.* **1983**, *261*, 215−223.

(14) Matsushita, Y.; Choshi, H.; Fujimoto, T.; Nagasawa, M. Preparation and Morphological Properties of a Triblock Copolymer of the ABC Type. *Macromolecules* **1980**, *13*, 1053−1058.

(15) Matsushita, Y.; Yamada, K.; Hattori, T.; Fujimoto, T.; Sawada, Y.; Nagasawa, M.; Matsui, C. Morphologies of ABC-Type Triblock Copolymers with Different Compositions. *Macromolecules* **1983**, *16*, 10−13.

(16) Cavicchi, K. A.; Berthiaume, K. J.; Russell, T. P. Solvent Annealing Thin Films of Poly(Isoprene-*b*-Lactide). *Polymer* **2005**, *46*, 11635−11639.

(17) Knoll, A.; Magerle, R.; Krausch, G. Phase Behavior in Thin Films of Cylinder-Forming ABA Block Copolymers: Experiments. *J. Chem. Phys.* **2004**, *120*, 1105.

(18) Di, Z.; Posselt, D.; Smilgies, D. M.; Papadakis, C. M. Structural Rearrangements in a Lamellar Diblock Copolymer Thin Film during Treatment with Saturated Solvent Vapor. *Macromolecules* **2010**, *43*, 418−427.

(19) Chavis, M. A.; Smilgies, D.-M.; Wiesner, U. B.; Ober, C. K. Widely Tunable Morphologies in Block Copolymer Thin Films Through Solvent Vapor Annealing Using Mixtures of Selective Solvents. *Adv. Funct. Mater.* **2015**, *25*, 3057−3065.

(20) Albert, J. N. L.; Epps, T. H. Self-Assembly of Block Copolymer Thin Films. *Mater. Today* **2010**, *13*, 24−33.

(21) Yu, X.; Peng, J.; Cui, L.; Wang, H.; Li, B.; Han, Y. Morphology Development of Ultrathin Symmetric Diblock Copolymer Film via Solvent Vapor Treatment. *Macromolecules* **2004**, *37*, 7301−7307.

(22) Knoll, A.; Horvat, A.; Lyakhova, K. S.; Krausch, G.; Sevink, G. J. A.; Zvelindovsky, A. V.; Magerle, R. Phase Behavior in Thin Films of Cylinder-Forming Block Copolymers. *Phys. Rev. Lett.* **2002**, *89*, 355011−355014.

(23) Zettl, U.; Knoll, A.; Tsarkova, L. Effect of Confinement on the Mesoscale and Macroscopic Swelling of Thin Block Copolymer Films. *Langmuir* **2010**, *26*, 6610−6617.

(24) Peng, J.; Kim, D. H.; Knoll, W.; Xuan, Y.; Li, B.; Han, Y. Morphologies in Solvent-Annealed Thin Films of Symmetric Diblock Copolymer. *J. Chem. Phys.* **2006**, *125*, No. 064702.

(25) Jung, Y. S.; Ross, C. A. Solvent-Vapor-Induced Tunability of Self-Assembled Block Copolymer Patterns. *Adv. Mater.* **2009**, *21*, 2540−2545.

(26) Li, Y.; Huang, H.; He, T.; Gong, Y. The Effect of the Preferential Affinity of the Solvent on the Microstructure of Solution-Cast Block Copolymer Thin Films. *J. Phys. Chem. B* **2010**, *114*, 1264−1270.

(27) Bang, J.; Kim, B. J.; Stein, G. E.; Russell, T. P.; Li, X.; Wang, J.; Kramer, E. J.; Hawker, C. J. Effect of Humidity on the Ordering of PEO-Based Copolymer Thin Films. *Macromolecules* **2007**, *40*, 7019−7025.

(28) Guo, Q. *Polymer Morphology: Principles, Characterization, and Processing*; John Wiley & Sons, Inc., 2016; pp. 1−445, DOI: 10.1002/9781118892756.

(29) Ullal, C. K.; Schmidt, R.; Hell, S. W.; Egner, A. Block Copolymer Nanostructures Mapped by Far-Field Optics. *Nano Lett.* **2009**, *9*, 2497−2500.

(30) Gong, W. L.; Yan, J.; Zhao, L. X.; Li, C.; Huang, Z. L.; Tang, B. Z.; Zhu, M. Q. Single-Wavelength-Controlled In Situ Dynamic Super-Resolution Fluorescence Imaging for Block Copolymer Nanostructures via Blue-Light-Switchable FRAP. *Photochem. Photobiol. Sci.* **2016**, *15*, 1433−1441.
(31) Purohit, A.; Centeno, S. P.; Wypysek, S. K.; Richtering, W.; Wöll, D. Microgel PAINT − Nanoscopic Polarity Imaging of Adaptive Microgels without Covalent Labelling. *Chem. Sci.* **2019**, *10*, 10336−10342.
(32) Conley, G. M.; Nöjd, S.; Braibanti, M.; Schurtenberger, P.; Scheffold, F. Superresolution Microscopy of the Volume Phase Transition of PNIPAM Microgels. *Colloids Surf., A* **2016**, *499*, 18−23.
(33) Chapman, D. V.; Du, H.; Lee, W. Y.; Wiesner, U. B. Optical Super-Resolution Microscopy in Polymer Science. *Prog. Polym. Sci.* **2020**, *111*, No. 101312.
(34) Dhiman, S.; Andrian, T.; Santiago Gonzalez, B.; Tholen, M. M. E.; Wang, Y.; Albertazzi, L. Can Super-Resolution Microscopy Become a Standard Characterization Technique for Materials Chemistry? *Chem. Sci.* **2022**, *13*, 2152−2166.
(35) Qiang, Z.; Wang, M. 100th Anniversary of Macromolecular Science Viewpoint: Enabling Advances in Fluorescence Microscopy Techniques. *ACS Macro Lett.* **2020**, *9*, 1342−1356.
(36) Tinnefeld, P.; Eggeling, C.; Hell, S. W. *Far-Field Optical Nanoscopy*, Vol. *14*; Wolfbeis, O. S., Ed.; Springer, 2015.
(37) Karanastasis, A. A.; Zhang, Y.; Kenath, G. S.; Lessard, M. D.; Bewersdorf, J.; Ullal, C. K. 3D Mapping of Nanoscale Crosslink Heterogeneities in Microgels. *Mater. Horiz.* **2018**, *5*, 1130−1136.
(38) Chan, J. M.; Kordon, A. C.; Zhang, R.; Wang, M. Direct Visualization of Bottlebrush Polymer Conformations in the Solid State. *PNAS* **2021**, *118*, No. e2109534118.
(39) Rust, M. J.; Bates, M.; Zhuang, X. Sub-Diffraction-Limit Imaging by Stochastic Optical Reconstruction Microscopy (STORM). *Nat. Methods* **2006**, *3*, 793−796.
(40) Albertazzi, L.; van der Zwaag, D.; Leenders, C. M. A.; Fitzner, R.; van der Hofstad, R. W.; Meijer, E. W. Probing Exchange Pathways in One-Dimensional Aggregates with Super-Resolution Microscopy. *Science* **2014**, *344*, 491−495.
(41) Chapman, D. V.; Hinckley, J. A.; Erstling, J. A.; Estroff, L. A.; Wiesner, U. B. Orthogonal Nanoprobes Enabling Two-Color Optical Super-Resolution Microscopy Imaging of the Two Domains of Diblock Copolymer Thin Film Nanocomposites. *Chem. Mater.* **2021**, *33*, 5156−5167.
(42) Hinckley, J. A.; Chapman, D. V.; Hedderick, K. R.; Oleske, K. W.; Estroff, L. A.; Wiesner, U. B. Quantitative Comparison of Dye and Ultrasmall Fluorescent Silica Core-Shell Nanoparticle Probes for Optical Super-Resolution Imaging of Model Block Copolymer Thin Film Surfaces. *ACS Macro Lett.* **2019**, *8*, 1378−1382.
(43) Li, Z.; Hur, K.; Sai, H.; Higuchi, T.; Takahara, A.; Jinnai, H.; Gruner, S. M.; Wiesner, U. Linking Experiment and Theory for Three-Dimensional Networked Binary Metal Nanoparticle−Triblock Terpolymer Superstructures. *Nat. Commun.* **2014**, *5*, 1−10.
(44) Erstling, J. A.; Hinckley, J. A.; Bag, N.; Hersh, J.; Feuer, G. B.; Lee, R.; Malarkey, H. F.; Yu, F.; Ma, K.; Baird, B. A.; Wiesner, U. B. Ultrasmall, Bright, and Photostable Fluorescent Core-Shell Aluminosilicate Nanoparticles for Live-Cell Optical Super-Resolution Microscopy. *Adv. Mater.* **2021**, *33*, 2006829.
(45) van Blaaderen, A.; Kentgens, A. P. M. Particle Morphology and Chemical Structure of Colloidal Silica Spheres Made from Alkoxysilanes. *J. Non-Cryst. Solids* **1992**, *149*, 161−178.
(46) Ovesný, M.; Křížek, P.; Borkovec, J.; Švindrych, Z.; Hagen, G. M. ThunderSTORM: A Comprehensive ImageJ Plug-in for PALM and STORM Data Analysis and Super-Resolution Imaging. *Bioinformatics* **2014**, *30*, 2389−2390.
(47) Susca, E. M.; Beaucage, P. A.; Hanson, M. A.; Werner-Zwanziger, U.; Zwanziger, J. W.; Estroff, L. A.; Wiesner, U. Self-Assembled Gyroidal Mesoporous Polymer-Derived High Temperature Ceramic Monoliths. *Chem. Mater.* **2016**, *28*, 2131−2137.
(48) Brinker, C. J.; Hurd, A. J.; Schunk, P. R.; Frye, G. C.; Ashley, C. S. Review of Sol-Gel Thin Film Formation. *J. Non-Cryst. Solids* **1992**, *147-148*, 424−436.
(49) Hurd, A. J.; Jeffrey Brinker, C. Sol-Gel Film Formation by Dip Coating. *MRS Online Proc. Libr.* **1990**, *180*, 575−581.
(50) Crossland, E. J. W.; Kamperman, M.; Nedelcu, M.; Ducati, C.; Wiesner, U. B.; Smilgis, D.-M.; Toombes, G. E. S.; Hillmyer, M. A.; Ludwigs, S.; Steiner, U.; Snaith, H. J. A Bicontinuous Double Gyroid Hybrid Solar Cell. *Nano Lett.* **2009**, *9*, 2807−2812.
(51) Yu, F.; Zhang, Q.; Thedford, R. P.; Singer, A.; Smilgies, D.-M.; Thompson, M. O.; Wiesner, U. B. Block Copolymer Self-Assembly-Directed and Transient Laser Heating-Enabled Nanostructures toward Phononic and Photonic Quantum Materials. *ACS Nano* **2020**, *14*, 11273−11282.
(52) Park, I.; Lee, B.; Ryu, J.; Im, K.; Yoon, J.; Ree, M.; Chang, T. Epitaxial Phase Transition of Polystyrene-*b*-Polyisoprene from Hexagonally Perforated Layer to Gyroid Phase in Thin Film. *Macromolecules* **2005**, *38*, 10532−10536.
(53) Hoheisel, T. N.; Hur, K.; Wiesner, U. B. Block Copolymer-Nanoparticle Hybrid Self-Assembly. *Prog. Polym. Sci.* **2015**, *40*, 3−32.
(54) Zhang, Z.; Liu, G.; Bell, S. Synthesis of Poly(Solketal Methacrylate)-*block*-Poly(2-(Dimethylamino)Ethyl Methacrylate) and Preparation of Nanospheres with Cross-Linked Shells. *Macromolecules* **2000**, *33*, 7877−7883.
(55) Narrainen, A. P.; Pascual, S.; Haddleton, D. M. Amphiphilic Diblock, Triblock, and Star Block Copolymers by Living Radical Polymerization: Synthesis and Aggregation Behavior. *J. Polym. Sci., Part A: Polym. Chem.* **2002**, *40*, 439−450.
(56) Zhang, X.; Matyjaszewski, K. Synthesis of Well-Defined Amphiphilic Block Copolymers with 2-(Dimethylamino)Ethyl Methacrylate by Controlled Radical Polymerization. *Macromolecules* **1999**, *32*, 1763−1766.
(57) Xiao, G.; Hu, Z.; Zeng, G.; Wang, Y.; Huang, Y.; Hong, X.; Xia, B.; Zhang, G. Effect of Hydrophilic Chain Length on the Aqueous Solution Behavior of Block Amphiphilic Copolymers PMMA-*b*-PDMAEMA. *J. Appl. Polym. Sci.* **2011**, *124*, 202−208.
(58) Greenwald, R. B.; Choe, Y. H.; McGuire, J.; Conover, C. D. Effective Drug Delivery by PEGylated Drug Conjugates. *Adv. Drug Delivery Rev.* **2003**, *55*, 217−250.
(59) Webster, R.; Didier, E.; Harris, P.; Siegel, N.; Stadler, J.; Tilbury, L.; Smith, D. PEGylated Proteins: Evaluation of Their Safety in the Absence of Definitive Metabolism Studies. *Drug Metab. Dispos.* **2007**, *35*, 9−16.
(60) Rubinstein, M.; Colby, R. H. Ideal Chains. *In Polymer Physics*; Oxford University Press, 2003; pp. 49−96.
(61) Warren, S. C.; DiSalvo, F. J.; Wiesner, U. Nanoparticle-Tuned Assembly and Disassembly of Mesostructured Silica Hybrids. *Nat. Mater.* **2007**, *6*, 156−161.
(62) Schmidt, G.; Malwitz, M. M. Properties of Polymer−Nanoparticle Composites. *Curr. Opin. Colloid Interface Sci.* **2003**, *8*, 103−108.
(63) Qiang, Z.; Akolawala, S. A.; Wang, M. Simultaneous In-Film Polymer Synthesis and Self-Assembly for Hierarchical Nanopatterns. *ACS Macro Lett.* **2018**, *7*, 566−571.
(64) Winey, K. I.; Thomas, E. L.; Fetters, L. J. Ordered Morphologies in Binary Blends of Diblock Copolymer and Homopolymer and Characterization of Their Intermaterial Dividing Surfaces. *J. Chem. Phys.* **1991**, *95*, 9367−9375.
(65) Higuchi, T.; Sugimori, H.; Jiang, X.; Hong, S.; Matsunaga, K.; Kaneko, T.; Abetz, V.; Takahara, A.; Jinnai, H. Morphological Control of Helical Structures of an ABC-Type Triblock Terpolymer by Distribution Control of a Blending Homopolymer in a Block Copolymer Microdomain. *Macromolecules* **2013**, *46*, 6991−6997.
(66) Garcia, B. C.; Kamperman, M.; Ulrich, R.; Jain, A.; Gruner, S. M.; Wiesner, U. Morphology Diagram of a Diblock Copolymer−Aluminosilicate Nanoparticle System. *Chem. Mater.* **2009**, *21*, 5397−5405.
(67) Robbins, S. W.; Beaucage, P. A.; Sai, H.; Tan, K. W.; Werner, J. G.; Sethna, J. P.; DiSalvo, F. J.; Gruner, S. M.; van Dover, R. B.;

Wiesner, U. Block Copolymer Self-Assembly−Directed Synthesis of Mesoporous Gyroidal Superconductors. *Sci. Adv.* **2016**, *2*, No. e1501119.
(68) Axelrod, D. Total Internal Reflection Fluorescence Microscopy. *In Methods in Cell Biology, Biophysical Tools for Biologists: Vol. 2. In Vivo Techniques*; Correia, J. J., Detrich, H. W., Eds.; Academic Press, 2008; pp. 169−221, DOI: 10.1016/S0091-679X(08)00607-9.
(69) Shen, H.; Huang, E.; Das, T.; Xu, H.; Ellisman, M.; Liu, Z. TIRF Microscopy with Ultra-Short Penetration Depth. *Opt. Express* **2014**, *22*, 10728−10734.
(70) Schermelleh, L.; Ferrand, A.; Huser, T.; Eggeling, C.; Sauer, M.; Biehlmaier, O.; Drummen, G. P. C. Super-Resolution Microscopy Demystified. *Nat. Cell Biol.* **2019**, *21*, 72−84.
(71) Ullal, C. K.; Primpke, S.; Schmidt, R.; Böhm, U.; Egner, A.; Vana, P.; Hell, S. W. Flexible Microdomain Specific Staining of Block Copolymers for 3D Optical Nanoscopy. *Macromolecules* **2011**, *44*, 7508−7510.
(72) Kim, B. J.; Bang, J.; Hawker, C. J.; Kramer, E. J. Effect of Areal Chain Density on the Location of Polymer-Modified Gold Nanoparticles in a Block Copolymer Template. *Macromolecules* **2006**, *39*, 4108−4114.
(73) Bockstaller, M. R.; Lapetnikov, Y.; Margel, S.; Thomas, E. L. Size-Selective Organization of Enthalpic Compatibilized Nanocrystals in Ternary Block Copolymer/Particle Mixtures. *J. Am. Chem. Soc.* **2003**, *125*, 5276−5277.
(74) Kim, B. J.; Bang, J.; Hawker, C. J.; Chiu, J. J.; Pine, D. J.; Jang, S. G.; Yang, S.-M.; Kramer, E. J. Creating Surfactant Nanoparticles for Block Copolymer Composites through Surface Chemistry. *Langmuir* **2007**, *23*, 12693−12703.
(75) Zhao, Y.; Thorkelsson, K.; Mastroianni, A. J.; Schilling, T.; Luther, J. M.; Rancatore, B. J.; Matsunaga, K.; Jinnai, H.; Wu, Y.; Poulsen, D.; Fréchet, J. M. J.; Alivisatos, A. P.; Xu, T. Small-Molecule-Directed Nanoparticle Assembly towards Stimuli-Responsive Nanocomposites. *Nat. Mater.* **2009**, *8*, 979−985.
(76) Oleske, K. W.; Barteau, K. P.; Turker, M. Z.; Beaucage, P. A.; Estroff, L. A.; Wiesner, U. Block Copolymer Directed Nanostructured Surfaces as Templates for Confined Surface Reactions. *Macromolecules* **2017**, *50*, 542−549.

https://doi.org/10.1021/acs.macromol.2c01017
Macromolecules 2022, 55, 9452−9464